V International Conference on Simulation for Additive Manufacturing
Sim-AM 2025
F. Auricchio, M. Carraturo and S. Morganti (Eds)

MULTI-SCALE THERMAL MODELLING AND VARIABEL SCAN PARAMETER OPTIMIZATION FRAMEOWRK FOR HOMOGENEOUS AND PREDICTABLE PBF-LB AEROSPACE COMPONENTS

TIM P.A. KOENIS[*], SYLL VAN BOHEEMEN[*†], MARIA L. MONTERO-SISTIAGA[*] AND MARC J. DE SMIT[*]

[*] Royal Netherlands Aerospace Centre (NLR)
Voorsterweg 31, 8316 PR Marknesse
e-mail: tim.koenis@nlr.nl, web page: http://www.nlr.org/

[†] University of Twente (UT)
Faculty of Engineering Technology, Department of Design, Production and Management
De Horst W-242, Drienerlolaan 5, 7522 NB Enschede
web page: https://www.utwente.nl/

Key words: numerical simulations, additive manufacturing (AM), process optimization, multi-scale

Abstract. In this study, a process optimization framework built around a multi-scale modelling approach to predict and prevent heat accumulation in the Laser-based Powder Bed Fusion (PBF-LB) processes is presented. A combination of low fidelity thermal Finite Element Model (FEM) and an Analytical Melt Pool Model (AMPM) is employed to optimize local scan parameters and interlayer time (ILT). The framework is validated experimentally using a WE43 magnesium alloy benchmark component, demonstrating its effectiveness in mitigating local overheating and strongly reducing porosity formation. However, combining the low fidelity FEM optimization and AMPM optimizations requires further refinement to fully leverage their strengths and improve accuracy. This research contributes to the development of more reliable and predictable PBF-LB processes for critical aerospace applications.

1 INTRODUCTION

Laser based Powder Bed Fusion (PBF-LB) is often used to build complex, topology-optimised geometries to make maximum use of the freedom in design that PBF-LB offers. However, the often complex component geometry can significantly impact local thermal history of PBF-LB material during the PBF-LB process, resulting in varying microstructure and mechanical properties within PBF-LB components [1]. Therefore, mechanical properties can locally deviate strongly from the used material allowables, which can be problematic for the certification of critical aerospace applications [2], [3]. To fully leverage the freedom in design and optimization offered by the PBF-LB process, it is essential to predict and mitigate these geometry-induced variations in the microstructure and mechanical properties without restricting the design possibilities.

In previous work, this problem has been addressed by introducing and optimizing variable interlayer time (ILT) based on low-fidelity transient thermal finite element models (FEM) [4]. Additionally, low fidelity FEM was used to adjust regional laser power to limit manufacturing time while avoiding heat accumulation [5]. The largest shortcoming of these methods is that they are incapable of predicting and thus preventing local overheating phenomena. E.g. short vectors in sharp geometrical features can give

rise to significant heat accumulation within a single PBF-LB layer. In the PBF-LB process for magnesium alloys such as WE43 this was found to be problematic, resulting in significant key hole porosities in locally overheating regions [6]. To cover the heat accumulation within a layer, high fidelity models are required.

This study expands the variable scan parameter optimization framework by combining thermal modelling approaches on multiple scales, optimizing local scan parameters and ILT. In this optimization framework, FEM is used to determine interlayer temperatures and optimise ILT and local laser power, while an analytical model is used to predict and avoid overheating at a scan track level. The models are employed to optimise the PBF-LB process for a WE43 benchmark component with the aim to prevent heat accumulation at both the part scale and the melt-pool scale. The optimization framework is experimentally validated with measurements using a long wave infrared (LWIR) camera measuring interlayer temperatures. Furthermore, analysis of the porosity in the specimens is used to validate the effectiveness of the preventive measures countering local heat accumulation.

2 METHODS

To be able to predict and prevent both the heat accumulation occurring over the duration of multiple layers as well as the heat accumulation occurring within a layer, a multi-scale modelling approach has been employed. A process optimization framework is built around the modelling methods to locally optimise scan parameters and avoid heat accumulation, thereby ensuring a more homogeneous thermal history.

2.1 Modelling methods

The multi-scale modelling approach requires the ability to predict trends in heat accumulation and the effect of counter measures, such as laser power reduction and the introduction of wait time. Furthermore, the model should be able to analyse the component within a practical timeframe for process optimization purposes. Practically, this would require a total analysis time in the order of 1 hour for a single representative component of the order of 100 mm^3. Therefore the combination of low fidelity part scale thermal FEM is combined with well-known analytical methods at the melt pool scale, in this paper referenced as the analytical melt pool model (AMPM).

The part scale thermal FE model has been developed in ABAQUS, and is similar to the methods used in previous research on part scale process optimization methods [4], [5]. Figure 1 (a) displays a schematic overview of the thermal FE model. Elements are activated based on machine tool paths with time increments containing 10-50 PBF-LB layers per increment depending on the component size and desired model fidelity. Additionally, heat is applied to the activated layers based on the laser scan path, laser power and absorptivity of the material. The boundary conditions incorporated in the model are the convective and radiative heat loss on the evolving exposed top surface of the component, as well as heat loss to the powder bed and heat exchange with the heating element located below the baseplate. Heat loss to the powder bed is modelled through the use of heat transfer coefficient as described by Chiumenti et al. [7]. The heat exchange with the heating element is modelled in the same way. The temperatures for heat exchange are set to 40 °C for the powder bed and 115 °C for the heating element obtained through experimental measurements.

Due to the low fidelity approach of the thermal FE method, it cannot predict melt pool temperatures or steep thermal gradients characteristic to the PBF-LB process. However, this model can predict the global evolving temperature field at low computational cost. Figure 1 (b) shows the interlayer temperatures, temperatures just before scanning of the next layer, determined for a complex aerospace bracket. Using the part scale FE model, regions with significant overheating in this bracket can be observed within a simulation time of 50 minutes on 4 CPUs.

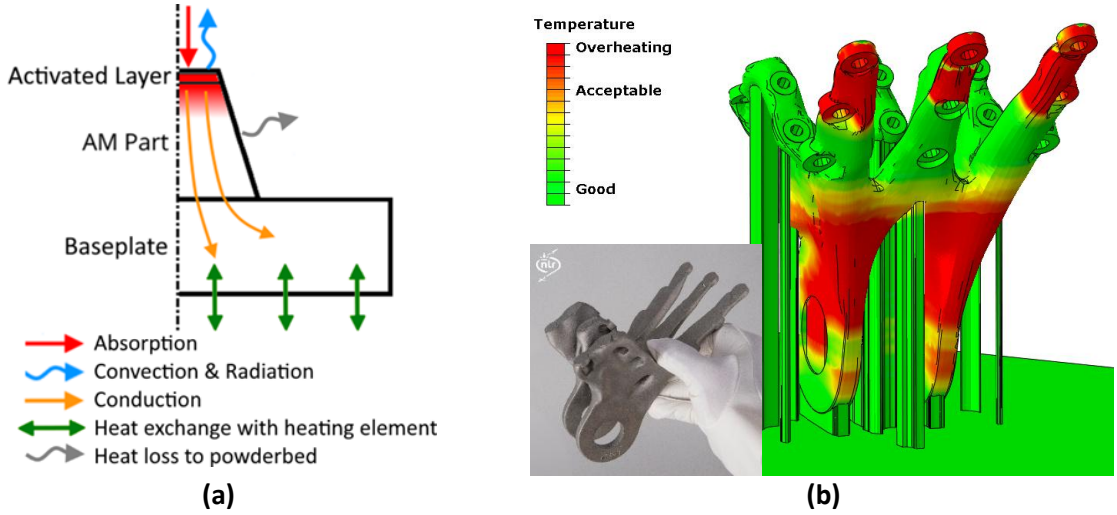

Figure 1: (a) schematic overview of the part scale thermal FE model and (b) interlayer temperature result for a complex aerospace bracket illustrating regions with significant heat accumulation

The AMPM is based on an analytical solution to the transient heat conduction equation which was derived with a moving Gaussian volumetric heat source developed for welding but also often used in modelling metal AM problems [8], [9]. This analytical solution was then implemented in python to simulate heat transfer along multiple linear tracks. Key assumptions are made to achieve this analytical equation, which includes treating the model as a semi-infinite domain (only finite in positive z-direction) and neglecting non-linear effects such as radiation and convection at the powder bed surface. Previous research has shown that with these adjustments a reasonable approximation of the heat transfer behaviour can still be made [10]. Assuming constant and uniform thermal properties for the classical transient heat conduction equation, and solving this for a moving heat source while assuming constant material properties, the temperature T at a point x_p and time t is given by:

$$T(t) = T_0 + \frac{2\eta Q}{\rho c (x/3)^{3/2}} \int_0^t \frac{1}{\sqrt{\phi_x \phi_y \phi_z}} exp\left(\frac{3x(t')^2}{\phi_x} - \frac{3y(t')^2}{\phi_y} - \frac{3z(t')^2}{\phi_z}\right) dt'$$

where T_0 is the initial temperature, η the absorption efficiency, Q the power of the laser, and the spatial offsets $x(t') = x_p - x_b(t')$, $y(t') = y - y_b(t')$, and $z(t') = z - z_b(t')$ represent the relative position between the point of interest and the heat source. The effective diffusion terms are $\phi_i = 12\alpha(t - t') + \sigma_i^2$, where $\alpha = k/\rho c$ is the thermal diffusivity and σ_i is the Gaussian distribution width in each spatial direction $i \in \{x, y, z\}$. Using this equation, the temperature distribution and melt pool generated by the heat source moving along an arbitrary scanning pattern of the laser can be modelled. Figure 2 illustrates an example of temperature distributions determined by the AMPM. Figure 2 (a) shows the scan pattern of the triangle. The melt pool and temperature distribution at points A and B are shown in Figure 2 (b) and (c) respectively. It can be observed that the AMPM predicts a significant increase in melt pool size at point B due to heat accumulation. It should be noted that no boundary conditions are imposed in the AMPM. Therefore, significantly more heat is lost to powder surrounding the scan pattern, limiting the amount of heat accumulation predicted by the AMPM. The same triangular shape was used to experimentally validate the AMPM for the magnesium WE43 alloy.

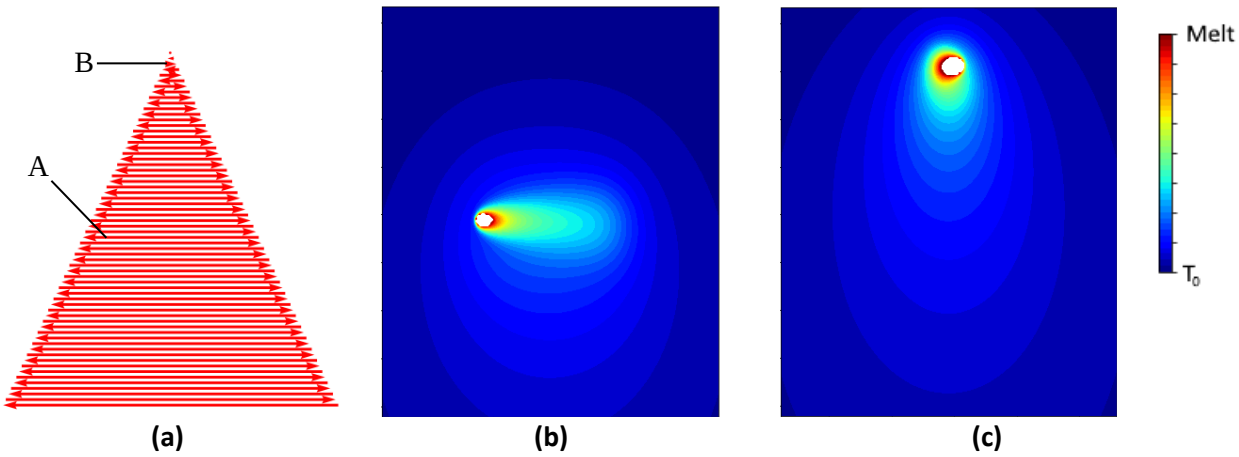

Figure 2: Snapshots of the temperature distribution in the top layer of a simple triangular prism in XY-plane (material: WE43) with: (a) the scanning pattern of the laser (b) temperature distribution when scanning point A and (c) temperature distribution when the laser is scanning point B

2.2 Optimization framework

To avoid heat accumulation on both the part scale as well as the layer scale, a combination of two process optimization frameworks was employed in python. First, the part scale models are used to prevent the heat accumulation based on interlayer temperatures obtained through thermal FEM. Afterwards, the model results and adjusted machine tool paths are fed into the framework for avoiding local overheating based on the AMPM.

The initial framework for PBF-LB process optimization at a part scale has been extensively discussed in previous research [4], [5]. Therefore, this method is only shortly described in this paper. The framework is built around the part scale FE models and can optimise the ILT for additional cooldown time where needed as well as adjust laser power regionally. Both methods ensure that the interlayer temperatures remain below a set limit temperature T_{lim}. The adjustment of laser power is preferred as this limits the need for additional built time. However, often geometry induced overheating would require significant scaling of laser power to be fully negated, increasing the change of lack of fusion. Therefore, the framework introduces ILT only when the required laser power drops blow a set threshold.

Figure 3 illustrates the different steps for the part scale optimization framework. As shown in Figure 3 (a), the model is initially split into control regions along the build direction. These regions are used to optimise the interlayer temperature based on the maximum interlayer temperature observed in the region. Additionally, each region is split into sub-regions as shown in Figure 3 (b). Each sub-region controls the sub-regional laser power based on the interlayer temperature measured at a control node near the centre of each sub-region. The sub-regional laser power control requires the division of the scan pattern to allocate the optimised laser power to the corresponding scan vectors. Figure 3 (c) displays the optimised laser power for a single layer showing how the optimization framework detects overheating sub-regions and lowers the laser power in these sub-regions. Figure 3 (d) displays the interlayer temperature field of a single region showing both the original interlayer temperature field containing overheating regions as well as the more homogeneous interlayer temperature field obtained employing the per sub-region optimised laser power. The initial round of process optimization can fully negate the occurrence of heat accumulation occurring over multiple PBF-LB layers. However, the heat accumulation occurring within a single layer, caused by the scan pattern and local conditions cannot be prevented in this way.

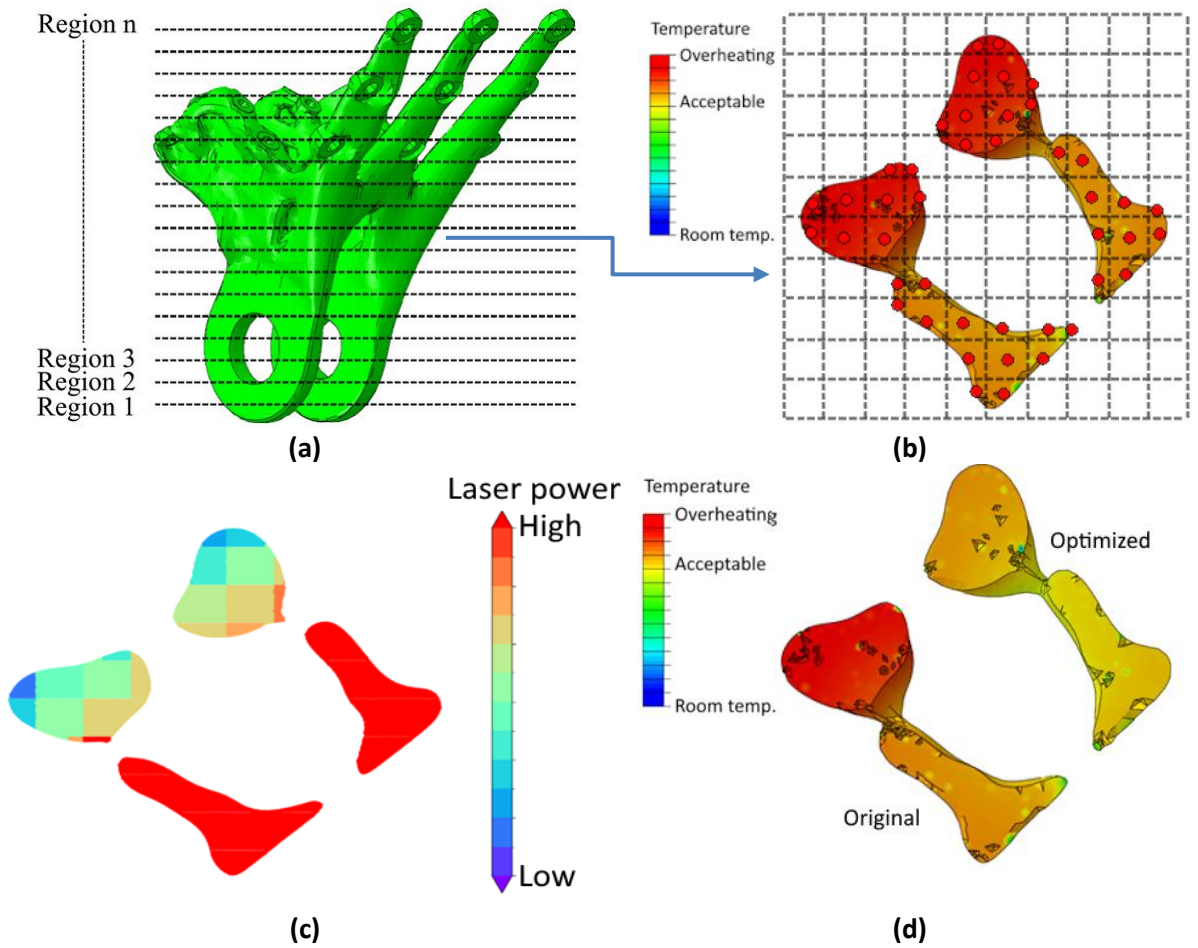

Figure 3: Steps in the part scale optimization with (a) discretization in regions of a complex component along the built direction, (b) discretization of a region into sub-regions with control nodes (c) adjusted sub-regional laser powers and (d) original vs optimised interlayer temperatures in a region of the complex component

To prevent local overheating within a layer, which can introduce defects and other part inhomogeneities, a second process analysis and adjustment was performed at the layer scale. This optimization loop employs the analytical method to estimate melt pool characteristics and adjust the laser power if these characteristics are out of bounds. The interlayer temperature per sub-region obtained from the final state of the part scale optimization combined with the scan pattern of the current layer is given as input for the optimization. The AMPM is used to determine the melt pool width in the middle of the scan vector per subsequent scan vector in the layer. If this width is too large, the laser power is iteratively scaled down using the Newton-Raphson method until a laser power is found that results in a melt pool width that falls within given bounds or the minimum laser power is reached. Once converged, the subsequent scan vector is analysed using an updated toolpath. This is shown for a simple triangular layer in Figure 4 (a). The scanning of this layer starts in a corner with very short vectors. Initially, no heat has accumulated, therefore no scaling of the laser power is required. However, as the scanning of the layer progresses, heat accumulates due to the short vectors, requiring scaling down of the laser power. Once the scan vector length starts increasing and the heat accumulation reduces, the laser power can be increased. However, when the pattern nears the other corner of the triangle and scan vector length reduces, the optimization framework scales the laser power back down again to avoid local overheating.

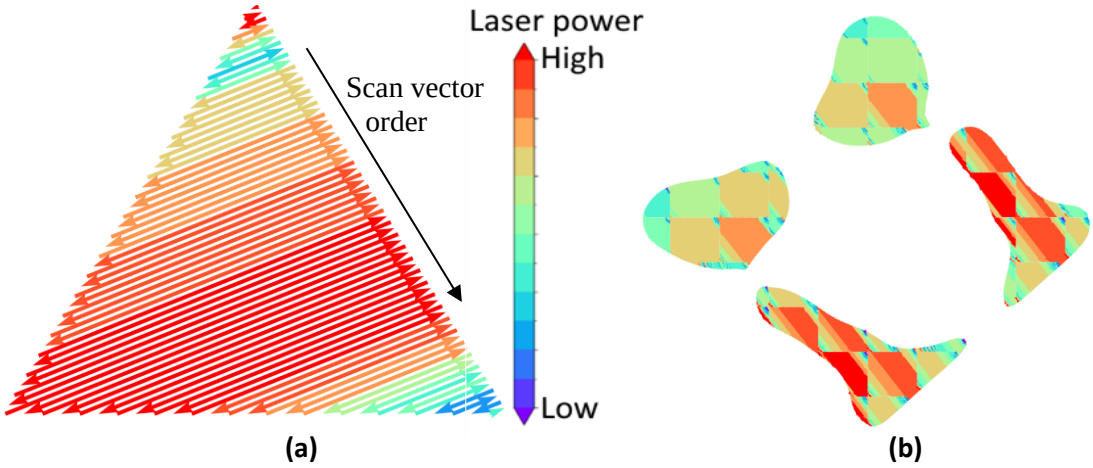

Figure 4: (a) optimised laser power per scan vector in a simple triangle and (b) the optimised laser power per scan vector in a complex PBF-LB layer

Figure 4 (b) displays the optimization of a more complex PBF-LB layer that was divided into sub-regions used in the part scale optimization. Here, the problems introduced by the splitting of the scan tracks in sub-regions becomes clear. Each sub-region contains corners where short vectors require significant adjustments of the laser power to prevent local heat accumulation, ensure more stable melt pool dimensions and avoid porosity formation.

Even though not exact, the analytical method can predict the overheating trends in a computationally efficient manner. The optimization of laser power of a single PBF-LB layer containing almost 3000 scan vectors is performed on a single core and finishes in 30 seconds. As each PBF-LB layer can be analysed individually, parallel computing is employed to improve the analysis time for the laser power optimization. Analysing and optimizing the representative aerospace bracket containing 3300 layers will thus cost approximately 1.5 hour on 20 CPUs.

2.3 Benchmark example

To experimentally test the combined PBF-PB process optimization framework to prevent heat accumulation over multiple layers and within a single layer, a small test component was defined. Figure 5 (a) displays a partly truncated tetrahedron placed with the truncated vertices facing downwards on 4 mm of support structures. This results in a component that has both an increasing cross sectional area in the build direction as well as sharp corners in every layer. These features are prone to both heat accumulation over multiple layers as well as within a layer. The component was produced in WE43 magnesium alloy which is prone to overheating and can show significant defect formation due to local heat accumulation. Figure 5 (b) displays the overheating observed in the component determined by the part scale thermal FE model. Table 1 displays the settings used for the boundary conditions and heat absorption in the FE model to model the PBF-LB process of WE43.

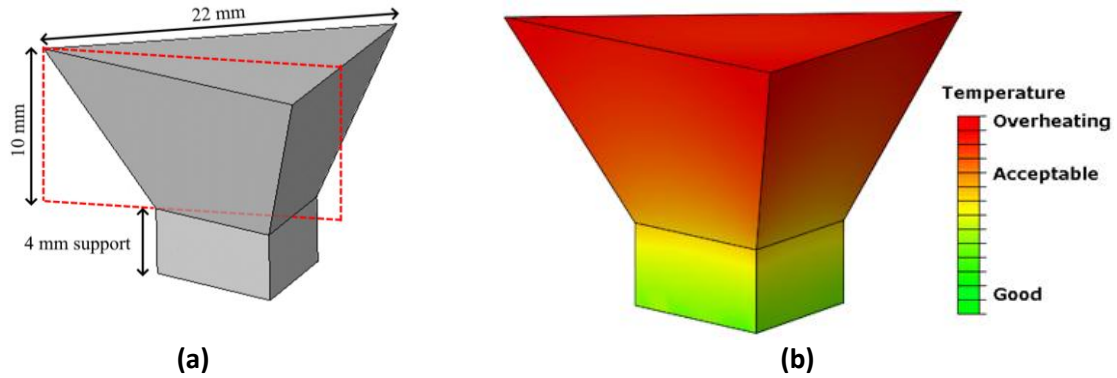

Figure 5: (a) the WE43 benchmark component and (b) the predicted overheating region in this component at part scale

Table 1: Calibrated settings for the FE process model for magensium WE43

Simulation parameter	Value [unit]
Absorptivity	0.55 [-]
Convection coefficient	12 [W/m^{2}K]
Emissivity	0.7 [-]
Heat transfer coefficient (powder)	2 [W/m^{2}K]
Heat transfer coefficient (baseplate)	90 [W/m^{2}K]

To experimentally validate the preventive heat accumulation methods, different combinations of the optimization framework were employed. The first specimen was produced as reference, and did not contain any preventive measures against heat accumulation. The second sample was manufactured using only the optimization framework based on the AMPM, using the analytical method to avoid overheating within each PBF-LB layer. The third specimen was manufactured using only the part scale optimization framework, which employs the FE model to estimate and prevent overheating by reducing the laser power. Finally, a fourth sample was manufactured that contains the combination of the FEM based and AMPM based optimization framework, aiming to avoid both heat accumulation over the height of the component as well as occurring within each layer. As the interlayer temperature was relatively uniform over each layer, only one sub-region was used for the FEM based optimization framework in specimens three and four.

The parts were fabricated on an SLM 280 dual laser PBF-LB machine with an nominal laser power of 154 W. The minimum allowed laser power used in the optimization framework was 100 W. During the PBF-LB process, interlayer temperatures are monitored by a LWIR camera measuring in the 7-12 µm range at 1 Hz with a resolution of 640 x 480 pixel resulting in a spatial resolution of approximately 0.5 mm per pixel. The LWIR camera was calibrated in a similar way as performed by Riensche et al. to ensure a good estimation of the interlayer temperature [11]. After manufacturing, cross-sections were made and polished for porosity analysis. The red dashed line in Figure 5 (a) displays the plane used for making the cross-section, going along the line from the tip of the triangle to the base and along the build direction.

3 RESULTS

Figure 6 displays the optimised scan paths of the final layer of the truncated tetrahedron specimen using the different optimization strategies. Figure 6 a-d show respectively the scan paths of the reference specimen, the specimen optimised based on only the AMPM framework to prevent local heat accumulation, the specimen optimised based on only the FEM framework to prevent layer wise heat

accumulation and the specimen optimised to prevent both layer wise and local heat accumulation. It is observed that the optimizations taking into account local effects scale down the laser power significantly when nearing the sharp corner with short vectors. Furthermore, the part scale optimization in Figure 6 (c) shows a significant reduction in overall laser power that is required to prevent layer wise overheating. The laser power throughout the final layer is as low as the minimum laser power used in the short vector region when using the AMPM based optimization framework. As shown in Figure 6 (d) the subsequent optimization to avoid local overheating largely overwrites the laser power imposed by the part scale optimization. This is because the local optimization tries to keep the melt pool as close to the target value as possible. The laser power optimised by the part scale model results in a melt pool that is smaller than the target width, causing the subsequent layer scale optimization to increase the laser power.

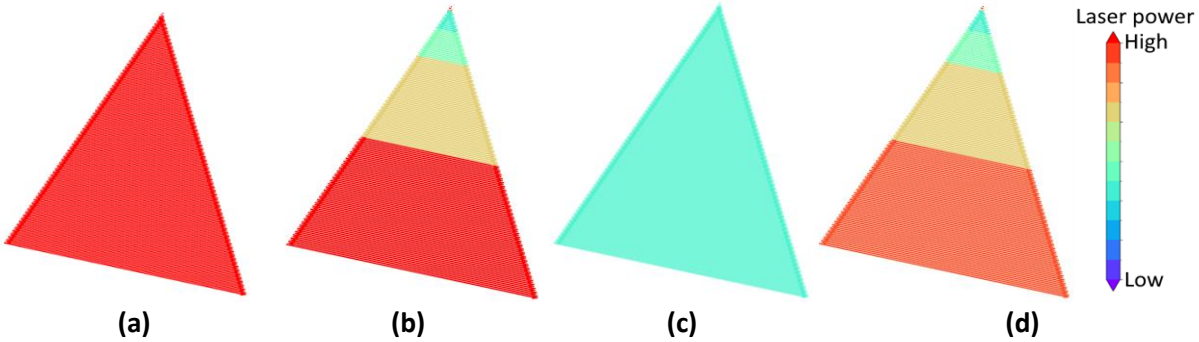

Figure 6: Laser power in the final layer of the WE43 benchmark with (a) nominal, (b) only optimised by AMPM, (c) only optimised by FEM and (d) optimised by FEM followed by AMPM

The effect of the different optimization strategies on the measured interlayer temperatures during the manufacturing of the specimens is shown in Figure 7. Here, it can be clearly seen that only the process optimised by employing the part scale simulation manages to keep the interlayer temperature below the set temperature limit T_{lim}. It is also shown that with the current optimization procedure combining the part scale and local scale fails to prevent part scale heat accumulation. This is caused by the overwriting of the FEM based optimization by the analytical model based optimization.

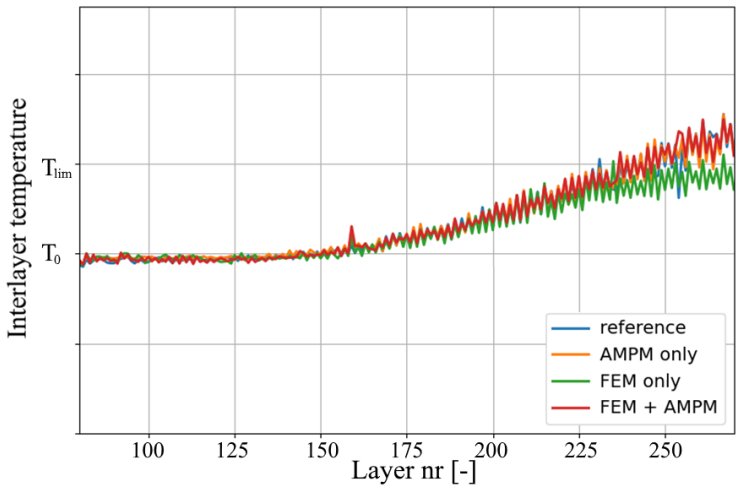

Figure 7: interlayer temperatures measured in the centre of each specimen by the full field LWIR camera

Figure 8 displays the cross-sections made of the four different specimens with a-d displaying the reference specimen, the specimen optimised by AMPM, the specimen optimised by FEM and the

specimen optimised by the combination of AMPM and FEM. Figure 8 (a) displays significant keyhole pore formation occurring in the sharp corner region where a large amount of short vectors cause significant local heat accumulation. By using the AMPM based optimization, either on its own or in combination with the FEM based optimization framework both fully negate the formation of key hole porosities in the sharp corner. Figure 8 (c) shows that initially large keyhole pores form in the specimen using the FEM based optimization framework. However, as this framework significantly scales down the laser power to levels similar as the AMPM framework, no keyhole porosities are observed in the upper 50 layers. Furthermore, no significant lack of fusion defects have been observed in the specimen using the FEM based optimization. This shows that even though the laser power is scaled down significantly, the melt pool geometry is still sufficiently large to ensure enough overlap between subsequent tracks and layers.

These results illustrate the need of incorporating methods to prevent local overheating in combination with the previously developed method of preventing layer wise heat accumulation. The current method of combining the FEM based and AMPM based optimization framework lacks the ability to successfully avoid layer wise heat accumulation. This can be improved by limiting the maximum laser power used by the AMPM to better align with the laser powers determined by the FEM based optimization framework. To this end, the lower limit of the melt pool width has to be determined to ensure no lack of fusion occurs.

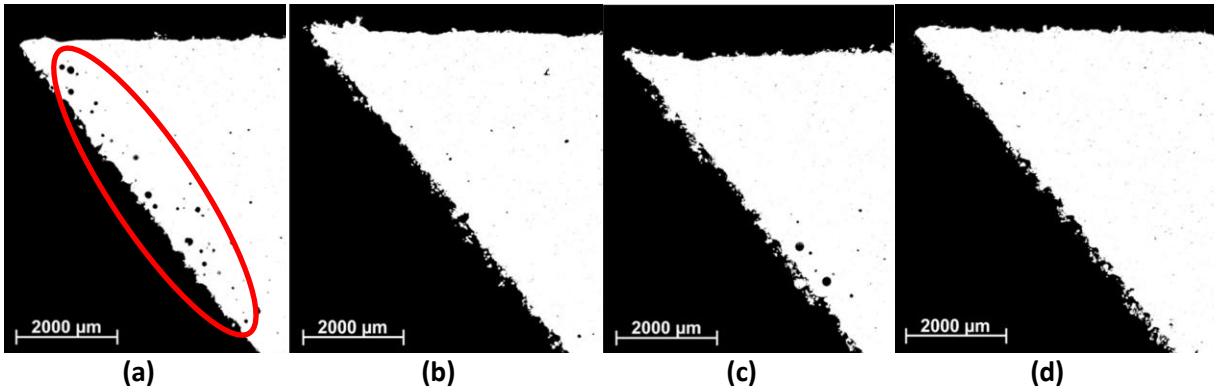

Figure 8: Porosity observed in the (a) reference, (b) AMPM only, (c) FEM only and (d) FEM+AMPM specimens

5 CONCLUSIONS AND FUTURE WORK

In conclusion, the multi-scale framework has been successfully demonstrated to predict heat accumulation trends at both part and layer scale. Even though the precision of the analytical melt pool model is limited in critical areas, it still effectively captures overheating phenomena. Process optimization using the analytical method mitigates overheating caused by the scan pattern at layer level, while optimization based on Finite Element Method (FEM) eliminates geometry induced overheating at part scale. However, combining the two methods primarily negates local overheating, as the part-scale FEM optimization is largely overwritten. Additionally, the current implementation of subregions required in the part-scale optimization causes additional overheating at the layer scale due to short vectors. Future work should focus on introducing more accurate methods for predicting local overheating while remaining computationally efficient. Furthermore, further investigating is required on the interplay between the AMPM optimization and the FEM optimization, improving subregion definitions to limit short vectors and improve the AMPM optimization to prevent it from largely overwriting the FEM optimization.

6 ACKNOWLEDGEMENTS

This research is conducted within the research and innovation program Luchtvaart in Transitie, which is co-funded by the Netherlands National Growth Fund.

REFERENCES

[1] G. Mohr, S. J. Altenburg, and K. Hilgenberg, 'Effects of inter layer time and build height on resulting properties of 316L stainless steel processed by laser powder bed fusion', *Addit. Manuf.*, vol. 32, p. 101080, Mar. 2020, doi: 10.1016/j.addma.2020.101080.

[2] J. Munk, E. Breitbarth, T. Siemer, N. Pirch, and C. Häfner, 'Geometry Effect on Microstructure and Mechanical Properties in Laser Powder Bed Fusion of Ti-6Al-4V', *Metals*, vol. 12, no. 3, Art. no. 3, Mar. 2022, doi: 10.3390/met12030482.

[3] P. Barriobero-Vila *et al.*, 'Mapping the geometry of Ti-6Al-4V: From martensite decomposition to localized spheroidization during selective laser melting', *Scr. Mater.*, vol. 182, pp. 48–52, June 2020, doi: 10.1016/j.scriptamat.2020.02.043.

[4] T. P. A. Koenis, M. L. Montero-Sistiaga, M. J. D. Smit, and E. Amsterdam, 'Simulation Based Process Optimization Towards Homogeneous Ti6Al4V components', doi: 10.23967/c.simam.2023.002.

[5] T. Koenis, E. Haumahu, M. Montero-Sistiaga, and M. de Smit, 'Model-Based Process Optimisation Framework for Variable Process Parameters Towards Homogeneous Ti-6Al-4V PBF-LB Aerospace Components', in *7th Fraunhofer Direct Digital Manufacturing Conference*, Berlin, Mar. 2025.

[6] M. J. de Smit, M. L. Montero-Sistiaga, and T. P. A. Koenis, 'Development of magnesium additive manufacturing for space applications', presented at the European Conference on Spacecraft Structures Materials and Environmental Testing, Noordwijk, The Netherlands, Sept. 2024.

[7] M. Chiumenti *et al.*, 'Numerical modelling and experimental validation in Selective Laser Melting', *Addit. Manuf.*, vol. 18, pp. 171–185, Dec. 2017, doi: 10.1016/j.addma.2017.09.002.

[8] N. T. Nguyen, A. Ohta, K. Matsuoka, N. Suzuki, and Y. Maeda, 'Analytical Solutions for Transient Temperature of Semi-Infinite Body Subjected to 3-D Moving Heat Sources', *Weld. Res. Suppl.*, pp. 265–274, 1999.

[9] B. Stump and A. Plotkowski, 'An adaptive integration scheme for heat conduction in additive manufacturing', *Appl. Math. Model.*, vol. 75, pp. 787–805, Nov. 2019, doi: 10.1016/j.apm.2019.07.008.

[10] P. Zagade, B. P. Gautham, A. De, and T. DebRoy, 'Analytical estimation of fusion zone dimensions and cooling rates in part scale laser powder bed fusion', *Addit. Manuf.*, vol. 46, p. 102222, Oct. 2021, doi: 10.1016/j.addma.2021.102222.

[11] A. Riensche *et al.*, 'Feedforward control of thermal history in laser powder bed fusion: Toward physics-based optimization of processing parameters', *Mater. Des.*, vol. 224, p. 111351, Dec. 2022, doi: 10.1016/j.matdes.2022.111351.